Ecological Modelling 397 (2019) 1–15

Contents lists available at ScienceDirect

Ecological Modelling

journal homepage: www.elsevier.com/locate/ecolmodel

Study on the emergy-based thermodynamic geography of the Jing-Jin-Ji region: Combined multivariate statistical data with DMSP-OLS nighttime lights data

Xueqi Wang[a], Gengyuan Liu[a,b,*], Luca Coscieme[c], Biagio F. Giannetti[a,d], Yan Hao[a,b], Yan Zhang[a,b], Mark T. Brown[a,e]

[a] State Key Joint Laboratory of Environment Simulation and Pollution Control, School of Environment, Beijing Normal University, Beijing 100875, China
[b] Beijing Engineering Research Center for Watershed Environmental Restoration & Integrated Ecological Regulation, Beijing 100875, China
[c] Post-graduation Program in Production Engineering, Paulista University, Rua Doutor Bacelar 1212, 04026002 São Paulo, Brazil
[d] Laboratório de Produção e Meio Ambiente, Programa de Pós-Graduação em Engenharia de Produção, Universidade Paulista, R. Dr. Bacelar 1212, Cep 04026-002, São Paulo, Brazil
[e] Center for Environmental Policy, Environmental Engineering Sciences, University of Florida, Gainesville, FL 32611, USA

ARTICLE INFO

Keywords:
Emergy
Spatialization
GIS
Thermodynamic geography
Nighttime lights data

ABSTRACT

Emergy analysis is one of the ecological thermodynamics methods. With a specific set of indicators, it is proved to be highly informative for sustainability assessment of national/regional economies. However, a large amount of data needed for its calculation are from official statistical data by administrative divisions. The spatialization of emergy in early researches were limited to the administrative boundaries. The emergy inside an administrative boundary renders a single value, which hides plenty of information for more precise regional planning.

This study develops a new methodology for mapping the spatial distribution of emergy density of a region. The renewable resource distribution can be mapped based on latest geospatial datasets and GIS technology, instead of solely relying on statistics and yearbooks data. Besides, a new spatialization method of non-renewable emergy based on DMSP-OLS nighttime lights data is proposed. Combined with the radiation calibration data, the problem of light saturation of DMSP-OLS nighttime lights data was solved to improve the emergy spatial detail of city centers. With a case study of Jing-Jin-Ji region, results showed that this method could generate a high-resolution map of emergy use, and depict human disturbance to the environment in a more precise manner. This may provide supportive information for more precise land use planning, strategic layout and policy regulation, and is helpful for regional sustainable development.

1. Introduction

1.1. Emergy analysis and its major difficulties in spatialization

Urban socio-economic systems have complex impacts on the environment. The formation and development of the city is based on the support by the surrounding natural environment. In regional planning and territorial management, we should not separate the urban areas from the surrounding natural areas. Instead, we should treat urban socio-economic and ecological systems as a whole (Huang, 1998). Emergy is a concept that can express the energy from the local and the offsite environment that supports it existence and development in terms of solar energy equivalents. It was proposed by H.T. Odum, based on the principles of thermodynamics and system ecology theory. It expresses the "solar equivalent energy" embodied in a product or a service, or the sum of direct and indirect inputs of all kinds of energy needed to generate a product or a service (Odum, 1971, 1988, 1996). Emergy of a nation/region takes into account all the renewable inputs (such as sunlight, wind, rain, geothermal heat) as well as the non-renewable inputs (such as fossil energy and mineral resources) of that nation/region. It establishes a unified dimension from an energy perspective, and allows combining the study of ecosystem and economic systems. From this point of view, emergy analysis has the advantage of being very informative in regional system study and planning, and has been widely used in regional scale (Fang and Ren, 2017; Li et al., 2014; Su et al., 2013).

* Corresponding author at: State Key Joint Laboratory of Environment Simulation and Pollution Control, School of Environment, Beijing Normal University, Beijing 100875, China.
E-mail address: liugengyuan@bnu.edu.cn (G. Liu).

https://doi.org/10.1016/j.ecolmodel.2019.01.021
Received 22 August 2018; Received in revised form 8 December 2018; Accepted 27 January 2019
Available online 05 February 2019
0304-3800/

By using emergy analysis, we can calculate the national/regional "solar equivalent energy" flow and obtain a series of indicators that reflect the ecological and economic characteristics of the system and evaluate its sustainable development capabilities. With the help of Geographic Information Systems (GIS) tools, by visualizing emergy and emergy-based indicators in space, policymakers can intuitively review the comparison and correlation between different areas, facilitate the adjustment of policies based on the characteristics of different regions, and promote the coordination and sustainable development within and between regions. Due to the data sources used for traditional emergy analysis are statistical data and yearbook data, most of the studies on the spatialization of emergy are based on administrative boundaries. For example, Sweeney Sweeney et al. (2007), developed a global national emergy accounting database (NEAD) and produced emergy distribution maps of major countries in the world. Pulselli et al. (2007) conducted an emergy zonal analysis for the Cagliari province (Italy); Li et al. (2014) and Yu et al. (2016) conducted an emergy analysis for 30 provinces in China and the Pearl River Delta region, respectively, comparing emergy indices at the provincial scale. However, by traditional mapping method, the emergy values are homogeneous in the same administrative region and the true emergy distribution in a regional scale are hidden. Pulselli (2010) pointed out that most of the studies that combined emergy analysis and geographic information systems were based on the boundaries of administrative regions. Within an administrative region, it is difficult to allocate emergy data at a high resolution. With the existing statistical data, the aggregation and dispersion of emergy in a region is difficult to understand and map, and thus emergy analysis becomes less informative as requirements of regional regulation and planning become more and more accurate. Emergy researchers have been increasingly aware of the importance of making more elaborate emergy distribution maps and have made many efforts. For example, Huang et al. (2001) applied the emergy calculation results of 1178 administrative districts in Taipei metropolitan region to the analysis of regional emergy spatial zoning map, which shows that the Taipei Basin has an energy spatial structure composed of six homogenous zones: mixed-use urban core, high density urban residential district, service and manufacturing urban district, agricultural district, newly developed suburban district, and natural area. Huang et al. (2018) used a variety of data downscale methods in the Beijing-Tianjin-Hebei urban agglomeration under the condition of data scarcity of city-level, and conducted spatialization of emergy according to the city boundary. Although the divisional scale is getting more and more detailed, it was still limited to the administrative boundaries.

With the progress of global ground monitoring, remote sensing technology, internet-based big data sharing and GIS technology, the method of spatialization of renewable emergy has gradually matured (Arbault et al., 2014; Lee and Brown, 2018; Mellino et al., 2014). However, for non-renewable emergy, producing a distribution map is still difficult because of the level of aggregation of the data. For example, data such as imports and exports, industrial production, etc., are usually obtained from the statistical data of administrative units. As a matter of fact, the non-renewable emergy for urban areas is quite vital because if accounts for most of the total emergy for cities since industrialization. The growth of cities' total emergy mainly depends on imported goods and services (Huang, 1998), and emergy inputs converge in the cities among a region. So a more precise non-renewable emergy spatial distribution for urban areas is quite worthy of study.

In previous studies, some researchers explored alternative methods to present the distribution of non-renewable emergy more precisely. Pulselli (2010) allocated statistical data of four provinces in the Abruzzo region of Italy to 315 cities based on population, area, or number of employees in each manufacturing department, and then used GIS's interpolation algorithm to generate non-administrative emergy distribution map with higher resolution. Huang et al. (2007) constructed energy flow models for different types of land use, and mapped the spatial heterogeneity of urban energy in the Taipei metropolitan region in 1 km × 1 km grids. Mellino et al. (2015) used transport systems and building distribution maps to map human-made capital in an attempt to represent the distribution of non-renewables. However, roads and buildings can only represent the emergy in storages of human-made capital, which do not reflect the flows of emergy.

1.2. Nighttime lights data provide the possibility of emergy spatialization

Under the condition that spatially distributed statistical data is difficult to obtain, researchers have found a strong correlation between regional nighttime lights data and non-renewable empower, which indicates that nighttime lights data may become a proxy measure for mapping the region's non-renewable emergy distribution map at a higher resolution (Coscieme et al., 2014; Mellino et al., 2013).

Nighttime lights data provides information about a complex, thermodynamics-based, aggregate measure of human activity. It has been widely used since they have been made available to the public. For example, nighttime lights data have been used to sketch city boundaries (Imhoff et al., 1997; Shi et al., 2014a). Many studies have shown that the lit area or brightness of lights is highly correlated with population density, GDP, energy consumption, carbon emissions, etc. (Doll et al., 2000; Elvidge et al., 1997a, 2001; Shi et al., 2014b).

Nighttime lights data can be used as an alternative estimation method for data that are hard to collect by the statistics department. For example, using nighttime lights data combined with statistical data such as GDP, energy consumption, etc. Chen (2015) estimated some social indicators such as infant mortality and poverty rates in some less-developed areas where the statistical census data is limited. When natural disasters occur, such as hurricanes, fires, earthquakes, or regional armed conflicts, it is difficult to obtain data on the ground. However, using nighttime lights satellites, power outages, electric power generation and transmission can be easily detected, and the impact of natural disasters, regional armed conflicts, etc. can be assessed (Coscieme et al., 2016; Elvidge et al., 1996).

Besides, it is possible to spatialize the statistical data that are difficult to spatialize otherwise at a higher resolution by using the correlation between nighttime lights data and socio-economic indicators. For example, nighttime lights data has been used to map economic activity intensity (Ghosh et al., 2010), carbon emission intensity (Rayner et al., 2010), spatial distribution of population (Doll, 2008; Sutton, 1997), electricity consumption (Townsend and Bruce, 2010), global poverty (Elvidge et al., 2009), impervious surface (Elvidge et al., 2007b), food demands (Matsumura et al., 2009), and steel usage in urban construction (Hsu et al., 2013), etc.

The two most widely used series of nighttime lights data are the DMSP-OLS dataset (available from 1992 to 2013), and the VIIRS dataset (available from October 2011 till now).

The US Air Force's Defense Meteorological Satellite Program (DMSP) Operational Linescan System (OLS) was originally designed for observing moonlit clouds (to collect meteorological information for US Air Force). Due to its high photoelectric amplification effect (gain effect), in addition to detecting clouds, it can detect low lights emitted by cities, gas flares, fires, even small-scale residential areas, traffic patterns, and fishing boats, which can be used as an indicator of human activity (Elvidge et al., 1997b; Elvidge et al., 2001). The satellites of the DMSP-OLS are sun-synchronous and circle the Earth 14 times a day. For night observations in various places, it usually passes through the sky from 20:30 to 21:30 at local time. The radiances in each cell of the light image is assigned a Digital Number (DN) value from 0 (meaning no light), to 63 (meaning the saturated light value), which means that the DNs found in the OLS data are relative values and not absolute light radiances.

In 1992, the National Geophysical Data Center (NGDC) of the National Oceanic and Atmospheric Administration (NOAA) established an electronic archive of DMSP-OLS data (Elvidge et al., 1999). Since then, it provided DMSP-OLS yearly nighttime lights data (from 1992 to

2013). The latest Version (V4) DMSP-OLS nighttime lights data can be downloaded from the NOAA-NGDC website (https://ngdc.noaa.gov/eog/dmsp.html). These data have a resolution of 30 arc-seconds, spanning from −180° to 180° longitude and −65° to 75° latitude, basically covering all human-inhabited regions on Earth (Bennett and Smith, 2017). The impacts of sunlight, moonlight, glares, clouds, and aurora have been screened out to enhance the quality of the data. The website provides nighttime lights data in four categories: cloud free coverage data, raw average data without noise removal, noise-removed stable light data, and average lights times percent frequency data. Among them, noise-removed stable light data are widely used as verifications or supplements of socio-economic statistical data (such as power consumption and GDP) (Amaral et al., 2005; Chand et al., 2009; Doll et al., 2000; Elvidge et al., 2001; Raupach et al., 2010). Fig. 1 shows the 2012 DMSP-OLS global stable light image obtained from the website. However, light saturation phenomenon is one of the main limitations of DMSP-OLS data. Due to the high gain settings and the limited range of detected radiation of the sensor, the DN value of OLS data usually appears saturated (DN = 63) in bright urban areas (Hsu et al., 2015). Study has shown that more than one-third of the urban areas in the United States present saturation values (Xie et al., 2014). The phenomenon of saturated lights makes some features of the central area of the city are not fully reflected, thus it reduces the availability of the data to present social and economic activities, and restricts the applicability of using light data for urban research (Elvidge et al., 2007a; Li et al., 2013).

The new generation Suomi NPP (VIIRS) nighttime lights data, with finer resolution and wider detection dynamic range, shows a stronger correlation with human activity indicators at more local scales (Elvidge et al., 2013). However, VIIRS is not superior to OLS in all aspects. For example, it can detect wavelengths in the range of 505–890 nm but does not include LED light below 500 nm. As some cities begin to switch from high-pressure sodium to more energy-efficient LED lighting, VIIRS will erroneously detect a reduction in light radiation (Falchi et al., 2016), while the wavelength range that OLS can detect is slightly wider (0.4 μm to 1.1 μm), and more LED lights can be detected. In addition, VIIRS observes the Earth's surface at about 1:30 a.m. local time (Bennett and Smith, 2017). At this time, human activities that use artificial lighting are generally fewer than what observed at 20:30 to 21:30. Therefore, we consider that OLS data is more suitable than VIIRS data for mapping regional emergy, since it has more abundant lighting information, and can depict human activities (such as energy consumption) more comprehensively.

Researchers have pointed out that the nighttime lights data is a reliable means to obtain the distribution of non-renewable emergy of a region (Coscieme et al., 2014; Mellino et al., 2013). However, they did not calibrate the urban lights in order to avoid the effect of saturation. Without correction, this may lead to loss of information of the emergy spatial distribution in light saturated areas.

This paper aims at enhancing the applicability of DMSP-OLS nighttime lights data for mapping non-renewable emergy for a region by applying a saturation correction method. Along with a direct GIS-based mapping method of renewable emergy, a methodological framework of emergy spatialization for a region is proposed. This method will provide a thermodynamics-based, metabolic geography of territorial systems and inform regional planning for sustainable development.

2. Material and methods

2.1. Case study area

In this paper, Jing-Jin-Ji region, also known as Beijing-Tianjin-Hebei, is selected as a research case to practice the method of regional emergy spatialization. Jing-Jin-Ji region belongs to the warm-temperate monsoon climate zone, which is located in the northern area of the North China Plain. It is surrounded by the Taihang Mountains and the Yanshan Mountains in the west and the north, and the coast of Bohai sea in the east, including two provincial cities Beijing and Tianjin, and 11 prefecture-level cities in Hebei province: Baoding, Cangzhou, Chengde, Handan, Hengshui, Langfang, Qinhuangdao, Shijiazhuang, Tangshan, Xingtai and Zhangjiakou. It covers an area of approximately 216,000 km^2, with a population of about 110 million. In 2012, the regional GDP was approximately 5.76 trillion yuan (Huang et al., 2018).

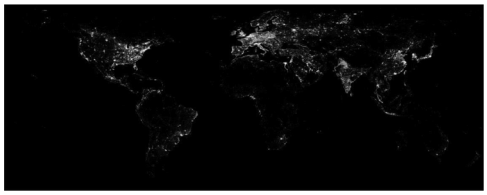

Fig. 1. The DMSP-OLS global stable light image for 2012 (adapted from https://ngdc.noaa.gov/eog/; last accessed July 2018).

Jing-Jin-Ji region is not only one of the largest and most developed areas in northern China, but also the strategic platform for China's economic growth, transformation and upgrading, and participation in global cooperation and competition in the new era. Since the reform and opening up, the Beijing-Tianjin-Hebei region has achieved remarkable achievements in the areas of economic development, social security, and transport infrastructure. But it also faces low levels of regional integration, lack of a regional organization of the labor system, and severe environmental problems. On the one hand, ecological vulnerability is prominent, and environmental issues have evolved from urban to regional ones. On the other hand, the development of urban systems has been unbalanced. Two big cities, Beijing and Tianjin, are the most developed, but the urbanization of secondary central cities has been slower. It can be seen from the land use map of the Jing-Jin-Ji region for 2012 (Fig. 2) that the residential and constructive areas in Beijing and Tianjin are larger, and the 11 prefectural cities in Hebei Province are smaller, where the main type of land use is cultivated land, forestland, and grassland. Breaking up the administrative divisions and studying the entire region as a whole, rather than each administrative unit, have been caught more and more attention[1] .

2.2. The emergy spatialization framework

This study establishes a framework to spatialize emergy of a given region (Fig. 3). The spatialization procedure is divided into two parts, the renewable part and the non-renewable part. Geospatial data provide data sources for the spatial distribution of regional environmental renewable resources, and geographic information systems (GIS) provide tools to calculate the corresponding emergy. Nighttime lights data are used to assign the non-renewable emergy spatially into each prefectural city. Beforehand, saturation correction method was applied to mitigate the light saturation phenomenon in city centers of DMSP-OLS data.

2.2.1. Data preparation

The available data are as follows. Non-renewable emergy data of the 13 cities in the study area for 2012 are acquired from the literature, which was calculated from statistical data (Huang et al., 2018). The geospatial datasets (renewable resources, nighttime lights datasets, and land use map) used in this study are listed in Table 1. The distribution of surface average solar radiance for Jing-Jin-Ji region was drawn by Zheng et al. (2012), which was based on the ground-based solar radiation observation data from 1998 to 2005. Davies (2013) developed a

[1] Here should be an announcement that the "city" here indicates the administrative unit of the government. In China, the government names the entire area within the administrative boundary "city", including urban areas, rural areas and natural areas.

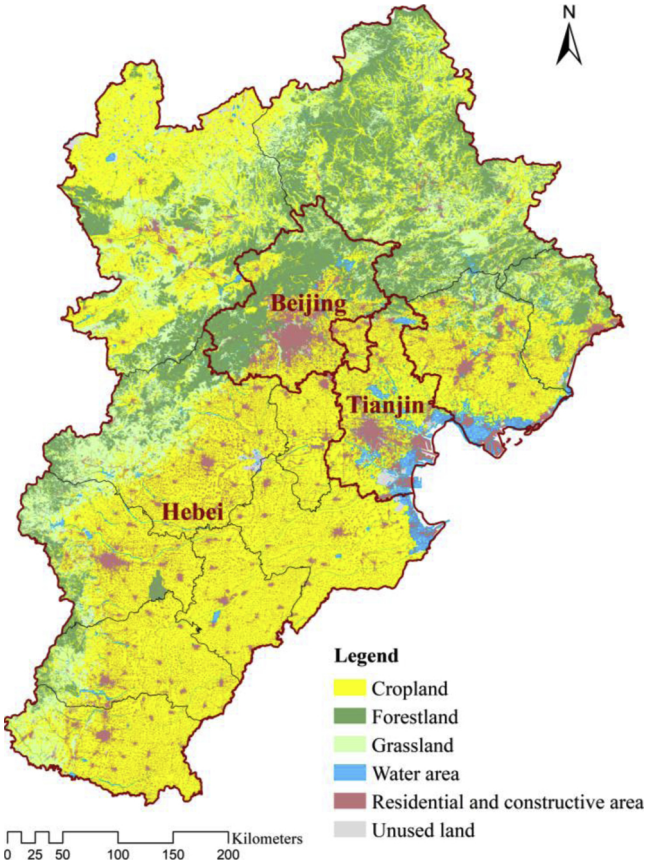

Fig. 2. Land use map of the Jing-Jin-Ji region for 2012.

global geothermal heat map based on 38,374 global heat flow measurement points around the world. Wind speed map is from the NASA's POWER (Prediction of Worldwide Energy Resources) Project Data Sets, which provides long-term average global wind speed at 50 m on a 0.5 arc degree resolution. Climatologies at High Resolution for the Earth's Land Surface Areas (CHELSA) dataset provides global raster data for monthly average precipitation from January 1979 to December 2013 with a resolution of 30 arc seconds. The CGIAR-CSI Global High-Resolution Soil-Water Balance dataset provides hydrological raster data describing actual evapotranspiration (AET) and soil water deficit with resolution of 30 arc seconds. The mean annual AET from 1950 to 2000 in this dataset is used in this study. The digital elevation coverage is from Jonathan de Ferranti, who developed and uploaded the whole world's digital elevation coverage maps at 3 and 15 arc second resolutions. DMSP-OLS stable lights data for 2012 and the radiance calibrated data for 2010–2011 can be downloaded at NOAA-NGDC websites. Land use data of Jing-Jin-Ji region of the year 2012 is from Resource and Environment Data Cloud Platform of Chinese Academy of Sciences (CAS).

All the spatial data are projected to the WGS_1984_UTM_Zone_50 N coordinates system. All the raster data are uniformed into 30 arc seconds (~700 m at the latitude of the study area; data with higher resolution are resampled, and data with lower resolution are re-gridded) for the convenience of calculation. The annual areal empower density is expressed in sej m^{-2} yr^{-1}.

2.2.2. *Spatialization of renewable emergy*

Renewable resources are the part of the natural support that flows into the regional system. Generally, the renewable inputs of a region include the tripartite (solar, tidal and geothermal), secondary and tertiary inputs (wind, rain chemical potential, runoff chemical potential and runoff geopotential). For a regional area which contains few or

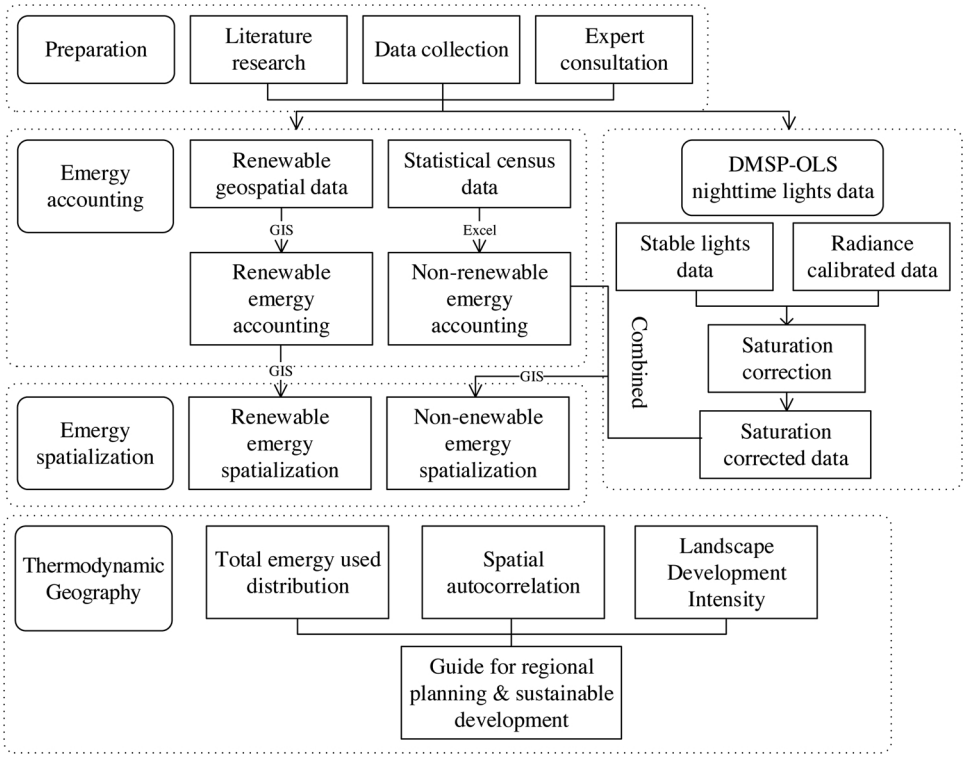

Fig. 3. Procedure used for emergy spatialization.

Table 1
Data sources for spatial datasets.

Data	Resolution	Source	Website
Solar	—	Zheng et al. (2012)	—
Geothermal	2°	Davies (2013)	http://onlinelibrary.wiley.com/doi/10.1002/ggge.20271/abstract
Wind speed	0.5°	NASA-POWER Project Data Sets	https://power.larc.nasa.gov/
Precipitation	30”	CHELSA	http://chelsa-climate.org/downloads/
AET	30”	CGIAR-CSI	http://www.cgiar-csi.org/data/global-high-resolution-soil-water-balance#disclaimers
DEM	15”	Developed and uploaded by Jonathan de Ferranti	http://viewfinderpanoramas.org/dem3.html
DMSP-OLS stable lights data	30”	NOAA-NGDC	https://ngdc.noaa.gov/eog/dmsp.html
DMSP-OLS radiance calibrated data	30”	NOAA-NGDC	https://ngdc.noaa.gov/eog/dmsp/download_radcal.html
Land use data	—	Resource and Environment Data Cloud Platform of CAS	www.resdc.cn

Table 2
Transformities used in this study.

Item	Transformity (sej/J)	Reference
Solar	1	Odum (1996)
Geothermal	4900	Brown and Ulgiati (2016)
Wind	680	Lee and Brown (2018)
Rain, chemical potential	10000	Lee and Brown (2018)
AET, chemical potential	10000	Lee and Brown (2018)
Runoff, geopotential energy	10000	Lee and Brown (2018)

none coastal areas, tidal energy and runoff chemical potential energy can be excluded. After the spatial data of every renewable resource was prepared, the ArcGIS tool “*Map Algebra*”, was used to calculate the available energy of each resource flowing into the system according to the energy calculation equations as follows. Then, the transformities (i.e. the conversion factors that account for the equivalent solar energy embodied in one unit of a product or service) were used to calculate emergy (Table 2), and the total renewable emergy of the system was calculated according to the rules of the emergy algebra.

2.2.2.1. Available energy (exergy) calculation method

2.2.2.1.1. Solar exergy. Using ground-based solar observation data, the solar radiation energy per unit area of the input system can be calculated according to Eq. (1);

$$E_{solar}(\mathrm{J/m^2 \bullet yr}) = I(\mathrm{J/m^2 \bullet yr}) \times (1 - A) \times K \quad (1)$$

where I is the observed solar radiation per unit area, A is the albedo (30%; Brown and Ulgiati (2016)), and K is the *Carnot* efficiency (0.93; Brown and Ulgiati (2016)).

2.2.2.1.2. Geothermal exergy. The surface heat flow energy distribution map is presented by Davies (2013) and an average Carnot efficiency of 69% (based on a weighted average of Carnot efficiencies for crustal, mantel and core sources) was used to converted to exergy (Lee and Brown, 2018).

2.2.2.1.3. Wind energy. The energy of the wind absorbed by the surface of each square meter is calculated by Eqs. (2) and (3) (Brown and Ulgiati, 2016);

$$V = V_{ref}\,(H/H_{ref})^{\alpha} \quad (2)$$

where V is the geostrophic wind speed, V_{ref} is the wind speed at the reference wind height, H_{ref} is the reference wind height (i.e.50 m), H is the geostrophic wind height (i.e.1000 m), and α is the surface roughness exponent (i.e. 0.25 for land surfaces; Manwell et al. (2010)).

$$E_{wind} = 1/2\rho K_{GN} V^3 T \quad (3)$$

Regarding Eq. (3), ρ is the air density $\approx 1.23\,\mathrm{kg/m^3}$,

K_{GN} is the geostrophic drag coefficient (i.e. 0.00164; Garratt (1992)), T = 31,536,000 s/yr (i.e. 31536000 s per year).

2.2.2.1.4. Rain (chemical potential) energy. In the mainland, the energy produced by rain is composed by two main elements: the energy generated by evapotranspiration (chemical) and the energy of runoff (physical). The chemical potential energy of water that is used by terrestrial vegetation within each cell is the water that is evapotranspired (Lee and Brown, 2018; Mellino et al., 2014).

The evapotranspiration energy can be obtained by multiplying the mass of rainwater evaporating in the area by the Gibbs free energy of rainwater (Eq. (4)), and the emergy distribution map of rain (chemical potential) is produced by multiplying the evapotranspiration chemical potential energy and its transformity;

$$E_{chem} = mG \quad (4)$$

where E_{chem} is the chemical potential energy in each cell of the raster data (i.e. the image), m is the mass of evapotranspired water from each cell, and G is the Gibbs free energy of rain (i.e. 4.723 J/g).

2.2.2.1.5. Runoff geopotential energy. Runoff can be calculated by the water budget equation;

$$R = P - E - I \quad (5)$$

where R accounts for the runoff, P for the precipitation, E for the evapotranspiration, and I for the infiltration.

In this study, it will be partially simplified that the infiltration is part of the runoff, so R = P-E, and the runoff map is generated by mapping the difference between precipitation data and evapotranspiration data.

Eq. (6) is used to obtain the geopotential energy of runoff;

$$E_{geopotential} = mgh \quad (6)$$

where $E_{geopotential}$ is the geopotential energy of runoff in each cell of the raster data, m is the mass of runoff in each cell, g is the acceleration due to gravity (9.8 $\mathrm{m/s^2}$) and h is the average altitude in each cell.

2.2.2.2. Renewable emergy maps. The emergy map of each renewable resource is obtained by multiplying its energy with its transformity. The renewable empower distribution map of the study area was generated by taking the maximum value between the sum of the solar, tidal and geothermal inputs and the largest of the secondary and tertiary inputs (wind, rain, runoff) for each cell, according to the algorithm developed by Brown and Ulgiati (2016), which can be expressed by Eq. (7). “*Cell Statistics*” tool in ArcGIS was used to extract the maximum value for each cell of the raster data.

$$Renewable = MAX\,[SUM\,(Solar,\ Geothermal,\ Tide),\ MAX\,(Wind,\ Rain,\ Runoff)] \quad (7)$$

2.2.3. Saturation correction method of DMSP-OLS data

Elvidge et al. (1999) firstly proposed a method of radiance calibration to correct the saturation of DMSP-OLS image. At high gain settings, the DMSP-OLS sensor can detect low lights, while urban centers are saturated. Turning the gain setting down can reduce the detected radiance. Therefore, different ranges of radiation could be obtained by setting different fixed-gains (15 dB, 35 dB, and 55 dB), and

Table 3
Eight global datasets from Global Radiance Calibrated Nighttime Lights Product.

Satellite name (Fxx; Fxx-Fyy for multiple satellites)	Earliest date and latest date of fixed-gain data that was used(yyyymmdd-yyyymmdd)
F16	20100111-20110731
F16	20100111-20101209
F16	20051128-20061224
F14	20040118-20041216
F14-F15	20021230-20031127
F12-F15	20000103-20001229
F12	19990119-19991211
F12	19960316-19970212

then different fixed-gain images were merged to generate a light image without saturation. This method directly adjusts the gain of the sensor and can resolve light saturation of the sensor from the source. It has also been continuously used and improved. Ziskin et al. (2010) improved the weighting method for different fixed-gain images' synthesis and made the splice of images more continuous and smooth, and produced the global radiation calibration light image for 2006. Hsu et al. (2015) presented an improved methodological framework for producing calibrated light images, which use the stable lights image as a supplement to the final radiation calibration image, to make up for the detection of some low lights may be missing since the quantity of images at fixed-gain settings is limited. A total of eight global datasets have been produced, representing years from 1996 to 2011 (Table 3; available at: https://ngdc.noaa.gov/eog/dmsp/download_radcal.html; last accessed on July 2018). But the gain setting approach is time and cost consuming, this method is unlikely to be used to correct the entire historical nighttime lights archive (Elvidge et al., 1999).

In order to compensate for the discontinuity of the radiation calibration product, researchers have proposed various methods for calibrating the saturation of DMSP-OLS nighttime light images in other ways. Hara et al. (2004) and Letu et al. (2010) applied linear regression model and cubic regression model respectively, which assumed that the DN value of the light increases linearly or cubically when approaching the light saturated center of the city. It was found that the correlation between the calibrated light data and the urban power consumption in several cities in Japan increased from $R^2 = 0.6876$ to $R^2 = 0.725$ and to $R^2 = 0.8264$ respectively. These methods assumed that the changes of lights in city centers followed certain mathematical models, which may

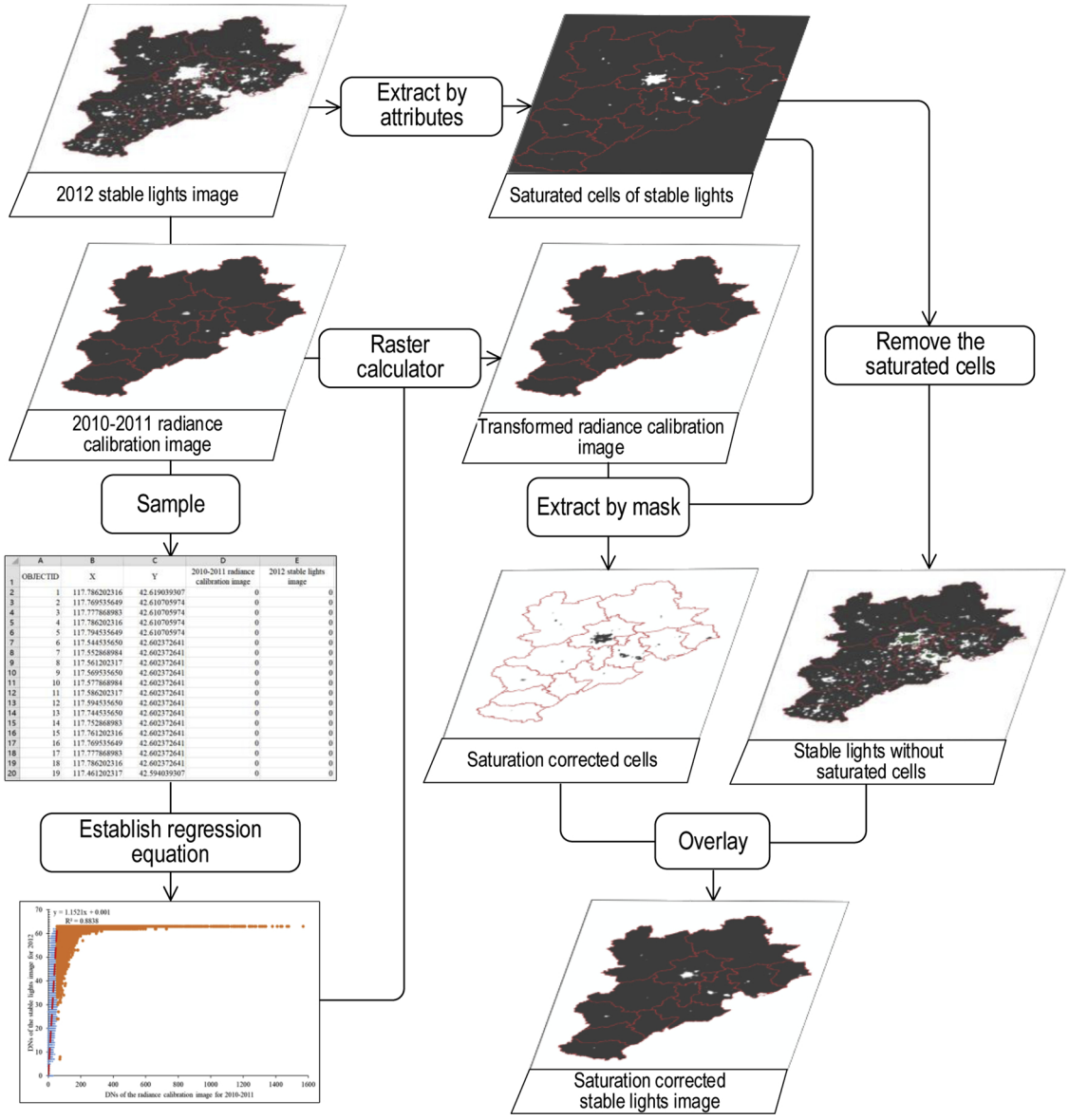

Fig. 4. The flowchart of stable lights correction method used in this study (after Letu et al., 2012).

cause that the light changes in the saturated areas are too idealistic on a micro level and were not widely used.

Lu et al. (2008) and Zhang et al. (2013) combined the Normalized Difference Vegetation Index (NDVI) from MODIS images and proposed HIS and VANUI methods respectively. They found correlations between urbanization level and vegetation health and abundance. Raupach et al. (2010) used population density to mitigate the saturation problem of nighttime light images around the world. After their correction, the correlations between the light data and GDP, energy consumption, and CO_2 emissions became stronger than the uncorrected ones. These methods can be used for correcting long-term time series of nighttime lights imagery. However, they require other data that describe human activities as supplements, which do not represent a direct solution to the problem of saturation. As we are going to study human activities from nighttime lights data, a direct calibration that does not rely on further external data is preferable.

Letu et al. (2012) sought to calibrate the saturated stable lights images using existing series of radiation calibration data (Table 3) with satisfactory results. They applied a certain mathematical method and GIS tools to calibrate the saturated pixels of the 1999 stable lights images by 1996–1997 radiation calibration data. The correlation between electricity consumption of several cities in Japan and its calibrated light data rose to $R^2 = 0.9273$, higher than by using other methods in the same study context. This paper applies this saturation correction method. The latest radiance calibration data is from Hsu et al. (2015) and the closest radiation calibrated data to 2012 stable lights data is the data from January 11, 2010 to July 31, 2011 (Table 3).

The flowchart of stable lights correction method is displayed in Fig. 4. In short, all the unsaturated lights data in 2012 stable lights image are kept, and the saturated part is replaced by the radiation calibrated data that after a regressive transformation.

The regressive transformation is used to transform the 2010–2011 radiation calibrated light image in order to minimize the light radiance difference from 2012 stable lights image. Using the "*Sample*" tool in ArcGIS and sampling every paired cell values at same location from the 2010–2011 radiation calibrated light image as well as the 2012 stable lights image, we discovered that the first saturated stable light (DN = 63) occurred when the radiation calibration light cell's DN value was 53.94. DN = 53.94 in the 2010–2011 calibrated image could be a saturation cut-off threshold. In other words, cells at the location of whose DN values are less than 53.94 in the 2010–2011 calibrated images are all unsaturated in the 2012 stable lights image. But it doesn't mean that cells at the location of whose DN values are higher than 53.94 in the 2010–2011 calibrated image are all saturated in the 2012 stable lights image. It means that the saturation phenomenon starts to appear in the 2012 stable lights image where the DN values are higher than 53.94 in the 2010–2011 calibrated image. The reason for this is the acquisition of stable lights images was based on satellites that could auto-adjust gain setting, which means that saturation does not occur immediately when the radiation reaches the detection limit. As the actual radiation increases, the DN value gradually shifts to the saturation value (Hsu et al., 2015). There are still unsaturated cells in the 2012 stable lights image where the DN values of cells are higher than 53.94 in the 2010–2011 calibrated image. But DN = 53.94 is the threshold that was used to establish the regression model of the stable lights cell values and radiance calibrated cell values at the same positions (R^2 = 0.88; Fig. 5). Then, the regression equation was used to transform the radiance calibrated data by using the "*Raster Calculator*" tool in ArcGIS.

The "*Extract by Attributes*" tool was used to extract the light saturated cells (DN = 63) from the 2012 stable lights image. Subsequently, a mask made up of these cells was used to extract the transformed radiance calibrated data at the corresponding position by the "*Extract by mask*" tool. The DN values of light saturated cells in stable lights data were turned into zero by the "*Raster Calculator*" tool. Finally, the extracted saturation corrected cells and the stable lights without saturated cells were overlaid to generate the saturation corrected stable lights image.

2.2.4. Spatialization of non-renewable emergy

Eq. (8) was used to spatialize the non-renewable emergy of each city in the study area;

$$y_{ij} = (x_{ij}/SOL_j)\cdot(N + I)_j \tag{8}$$

where j represents a city and i represents a raster cell in the city j ; y_{ij} is the non-renewable emergy of the i th cell in city j ; x_{ij} is the saturation corrected light value of the i th cell in city j ; $(N + I)_j$ is the non-renewable emergy of city j ; and SOL_j is the sum of lights of the saturation corrected stable lights of city j.

Thus, the non-renewable emergy was distributed to each cell of each city, and then the grid non-renewable emergy distribution data of each city in the urban agglomeration were spliced together to generate the non-renewable emergy distribution map of the urban agglomeration.

2.2.5. Thermodynamic geography indicators

2.2.5.1. Empower density. By summing up the renewable and the non-renewable empower, total empower distribution map of the study region can be produced. The values of the raster cells are summed up with the "*Raster Calculator*" tool in ArcGIS. The empower density of a city can be used as a development density parameter which can reflect the level of urbanization and the wealth of residents (Lee and Braham, 2017). We can also observe the different level of urban development better by making comparisons between cities. It should be noted that the boundary of "city" in China include urban areas, rural areas and natural areas. It may be different in other countries of the world, so we should pay attention to this issue when making such comparisons. In this study, the residential and constructive areas of Beijing, Tianjin, Hebei were extracted as "urban areas" by using land use map. Since the emergy baselines used in different years of researches can be different, the emergy data should be unified into a same baseline before comparison. In this study, the data were all reported to the latest 1.20E + 25 sej/yr emergy baseline (Brown et al., 2016).

2.2.5.2. Spatial autocorrelation. The "*Spatial Autocorrelation*" (Global Moran's *I*) tool in ArcGIS measures spatial autocorrelation based on feature locations and attribute values. Given a set of features and an associated attribute, the tool evaluates whether the pattern expressed by the features attributes is clustered, dispersed, or random. The Global Moran's *I* index is generally between −1 and 1. It indicates a clustered trend when the index value is positive, and the closer to 1 the more clustered. Negative index value indicates dispersed trend, and the closer to −1 the more dispersed. The tool calculates the Moran's *I* index value and both z-score and p-value to evaluate the significance of the results (Appendix A). We can quantify the aggregation extent of emergy spatially by the help of this index (Mitchell, 2005). The raster format data should be converted into features before using this tool.

2.2.5.3. Landscape development intensity index (LDI). LDI was proposed by Brown and Vivas (2005) and has been widely used to measure the gradients of human disturbance in wetlands (Carey et al., 2011; Zhang et al., 2014a, b). Areas with high levels of human disturbance are usually characterized by intensive material and energy consumption, human activities and environmental pollution.

In this paper, LDI index map is generated to see the spatial distribution characteristics of human disturbance gradients in the study area. LDI index for each cell of the map can be calculated by Eq. (9);

$$LDI_i = 10 \times log_{10}(U_i/R_i) \tag{9}$$

where U_i refers to the total (renewable plus non-renewable) empower of the i th cell, and R_i refers to the renewable empower of the i th cell.

The spatial variation coefficient (SVC) of LDI index of a region is the ratio of its standard deviation to its mean, which can measure the

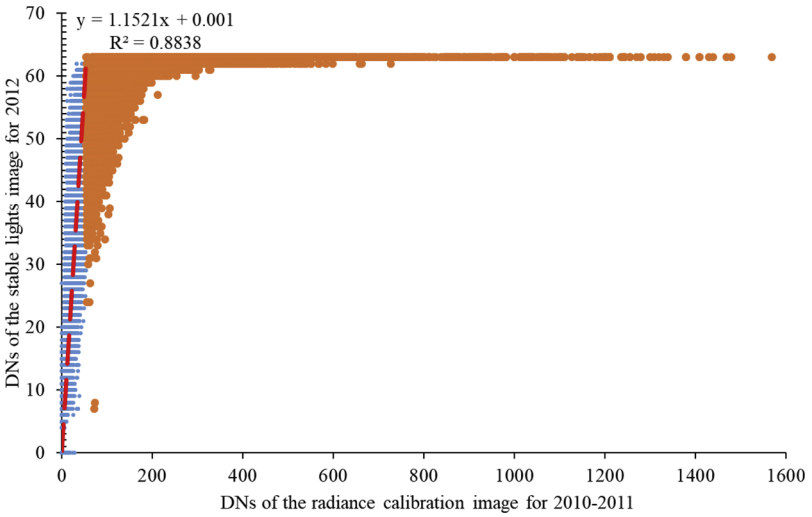

Fig. 5. Regression line used for the saturation correction of the 2012 stable lights image. The small dots on the left indicate non-saturated pixels (DN < 53.94); the big dots on the right indicate saturated pixels (DN > 53.94).

dispersion of the distribution of LDI index of a region. Because the standard deviation of data must always be understood in the context of the mean of the data, for comparison between data sets with different means, coefficient of variation is more comparable instead of the standard deviation. A lower spatial variation coefficient means a more evenly distributed of human disturbance, whereas a higher spatial variation coefficient means a more dispersed or unevenly distributed of human disturbance.

3. Results and discussions

3.1. Nighttime lights saturation correction and the non-renewable empower map

As a result of saturation correction, the DN range of the nighttime light imagery was expanded from the previous 0–63 to 0–1808.51 (Fig. 6b). Two night light profiles were created along an axis through the center of Beijing (Fig. 6), and the DN values of these two profiles are presented in Fig. 7, evidencing how much more detail can be gained through saturation correction. It can be seen that before the correction,

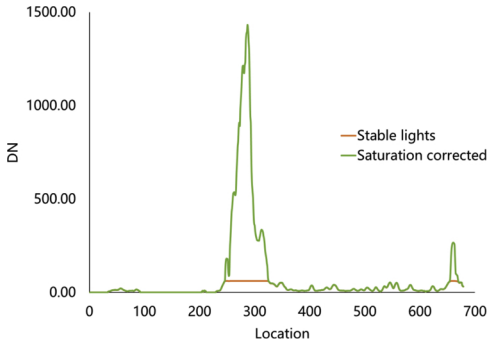

Fig. 7. Profiles of the stable lights data and saturation corrected data.

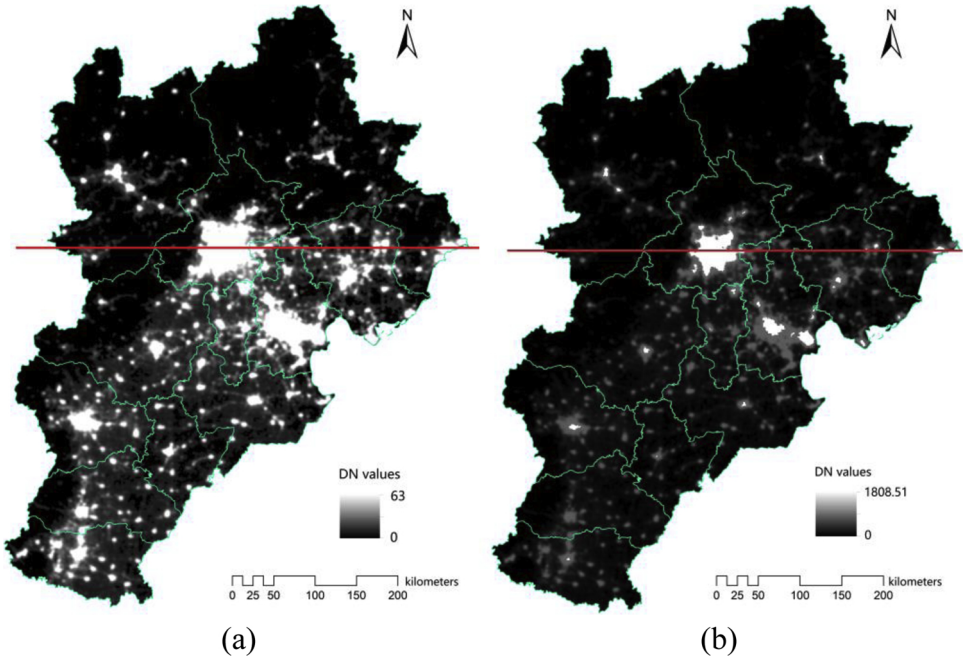

Fig. 6. (a) Stable lights and (b) saturation corrected images of the Jing-Jin-Ji region for the year 2012.

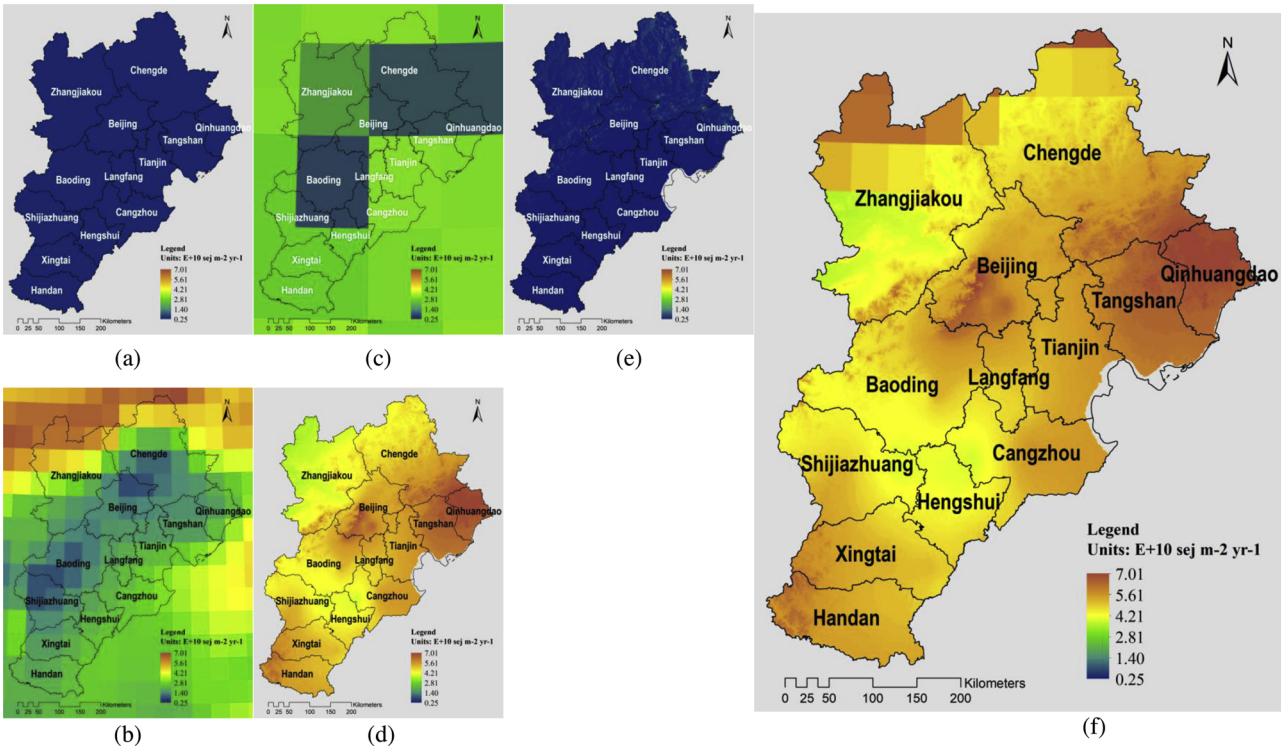

Fig. 8. Spatial distribution map of renewable emergy in the Jing-Jin-Ji region: (a) solar emergy; (b) wind emergy; (c) geothermal emergy; (d) rain (chemical potential) emergy; (e) runoff (geopotential) emergy; (f) total renewable emergy.

the central area of the city showed a saturation value of 63 in a large range. The dynamic characteristics of this part of the light were revealed after correction, where the maximum corrected DN value is 1432, nearly 23 times higher than the maximum DN value before correction. It is clear how light saturation correction is a crucial operational step, especially in cities where the saturated pixels occupy a large proportion of the city area. Saturation correction can greatly enrich the understanding and visualization of the thermodynamic spatial characteristics of urban centers.

3.2. Renewable empower maps

The emergy of renewable resources of the Jing-Jin-Ji region was spatialized, at a resolution of 30 arc second (Fig. 8). It can be seen that the renewable emergy in Jing-Jin-Ji region does not present a large spatial heterogeneity. The driving force of the renewable emergy at each location can be identified by the spatial analysis tool-*Highest Position* in ArcGIS. Under the influence of a typical monsoon climate, wind and rain are the dominant renewable resources of the region (Fig. 9). Wind emergy is prominent in the north of Zhangjiakou and Chengde, and rain (chemical potential) emergy is prominent in most other places in Jing-Jin-Ji region. Cities can be ranked based on the available renewable emergy, its density, and the average density of different land use types of the Jing-Jin-Jin region can be also ranked (Appendix B). It can be seen that Chengde and Zhangjiakou rank the top two of total renewable emergy. The flow of natural emergy in these two cities is relatively abundant, mainly because of their large land area, since the average density of renewable empowers of these two cities are not highly ranked. Although the total renewable emergy of Qinhuangdao is not highly ranked because of its limited area, it shows high values of renewable empower density. Langfang and Hengshui are characterized by the lowest two of renewable emergy. These cities have fewer natural resource availability and host less healthy environments compared to other cities in the region. Unused land has the highest renewable empower density values, followed by water area, forestland, residential

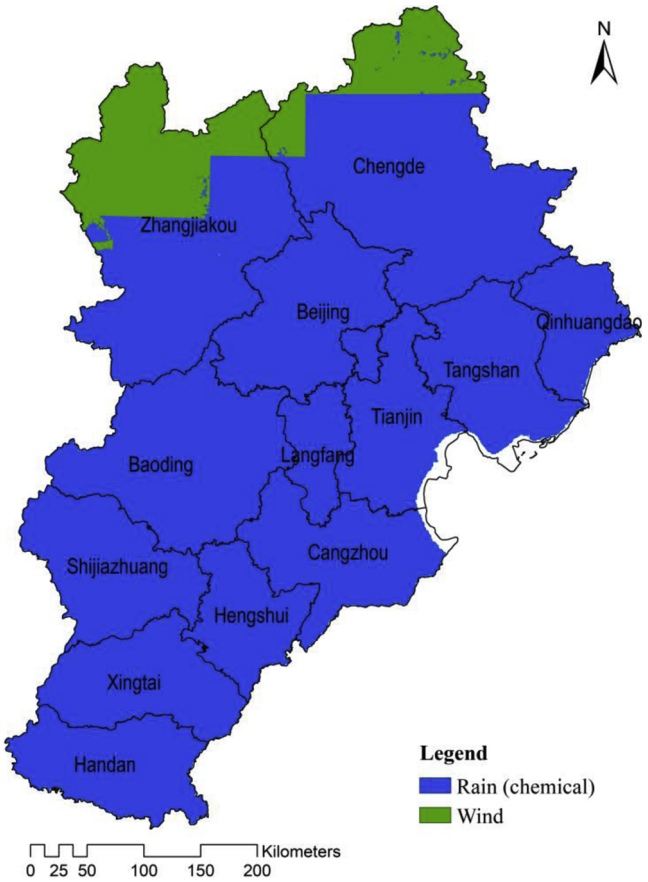

Fig. 9. Distribution of the main components of renewable emergy in the Jing-Jin-Ji region.

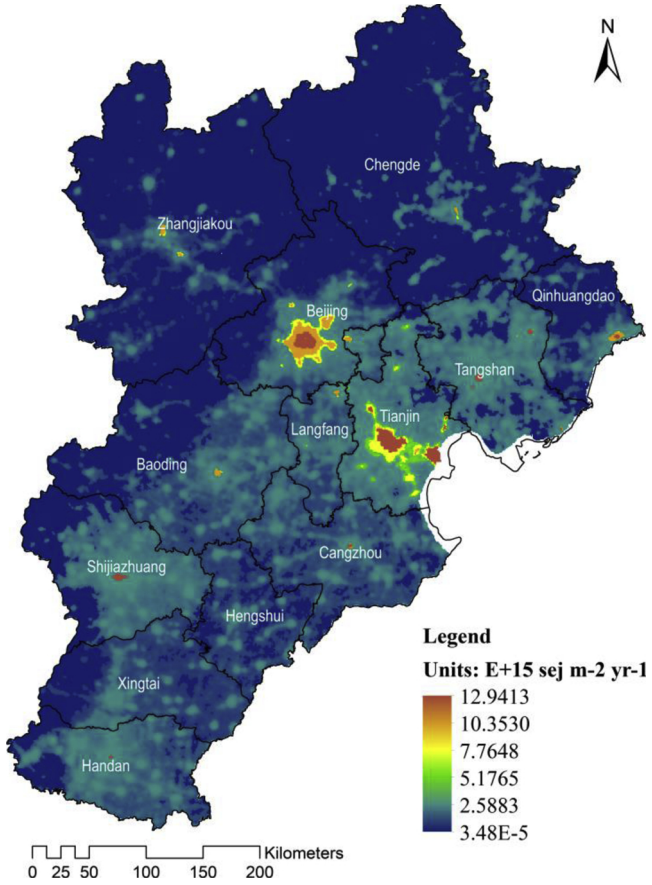

Fig. 10. Total emepower distribution in the Jing-Jin-Ji region for the year 2012.

and constructive area, and cropland ranks the lowest. These messages can assist a better energy and land use planning. For example, we can see the distribution of renewable resources and use them where appropriate; identifying ecosystems that with smaller renewable emergy might be relatively fragile, so it needs to be carefully protected; to maximize renewable resource availability, unused land should not be developed as residential and constructive area, etc.

3.3. Total empower density map

Total empower density map with a resolution of 30 arc second is shown in Fig. 10. It is almost the same as the non-renewable empower density map, because compared to non-renewable emergy (~E+14 sej m^{-2} yr^{-1}), the magnitude of renewable emergy (~E+10 sej m^{-2} yr^{-1}) is too small. There is nothing different when summing the renewable into the non-renewable (so non-renewable empower density map is not specifically displayed in this paper).

As we can see from Fig. 10, Beijing and Tianjin have the largest and the most concentrated emergy consumption in Jing-Jin-Ji region, which indicates that they are the most developed in this region. Beijing has one large empower concentration area in the city center, spreading outwards in a star shape; while Tianjin has two relatively independent emergy concentration areas in the city center and in the Binhai New Area. But we can also see that the empower density of the two areas of Tianjin is higher than that of Beijing, and has a tendency of connecting together as a whole. If it is not controlled, Tianjin has the danger of forming a big pie-like urban development like Beijing. Other cities in the Hebei province have much smaller emergy concentration areas at the city center or at the coastal area, and the empower density suddenly decreases outward from the concentration area, which shows that the sizes of the cities in Hebei province are much smaller and less developed.

Furthermore, we can make comparisons of the empower density between cities (Table 4). It can be seen that the empower density in the "urban area" of Tianjin (7.88E + 14) is the highest in the Jing-Jin-Ji region, a little higher than Macau (6.09E + 14), but lower than Manhattan, New York (2.28E + 15) and Harlem, New York (1.78E + 15). The Beijing "urban area" and province, the Tianjin province, and the Hebei "urban areas", have lower empower density than Macao, but larger than Rome (8.11E + 13) and Taipei (6.76E + 13). The Hebei province ranks the lowest (3.83E + 13) in terms of empower density, among the cities and areas investigated (Table 4). In the Jing-Jin-Ji region, the empower densities in all urban areas are much greater than within the city boundaries. In the Tianjin urban area, the emergy density is 2.42 times larger than its province. The same ratio is 3.43 in Beijing and 3.20 in Hebei. These results indicate that the level of urbanization and the wealth of residents of Tianjin "urban area" are close to the cities of developed countries, but there is still lots of room for improvement. Too much rural areas inside the city boundary in China have dragged down the total level of urbanization and the wealth of residents of the city.

3.4. Spatial Autocorrelation of total empower in Jing-Jin-Ji region

The Global Moran's *I* index of each city investigated is above 0.85, which indicates that the total empower of all the cities in the Jing-Jin-Ji region is very concentrated. Beijing, Tianjin and Qinhuangdao show the highest concentration (i.e. 0.982850, 0.962132 and 0.937601, respectively; Appendix C). The Global Moran's *I* of the entire region (including the areas of all the provinces) is 0.96, slightly smaller than the value for Tianjin. This indicates that the total emergy used in Beijing and Tianjin is not only very concentrated, but also very large. The results are statistically significant and all the confidence levels are greater than 99% (Appendix C).

Table 4
Empower density of cities and provinces in the Jing-Jin-Ji region and other cities from previous studies.

City(region)	Year	Empower desity sej/m^2/yr	References
Wall Street, New York	From multiple datasets of different years	3.60E+15	Lee and Braham (2017)
Manhattan Island, New York		2.28E + 15	Lee and Braham (2017)
Washington Heights, New York		1.94E+15	Lee and Braham (2017)
Harlem, New York		1.78E + 15	Lee and Braham (2017)
Urban areas of Tianjin	2012	7.88E + 14	This research
Macao	2004	6.09E + 14	Lei et al. (2008)
Urban areas of Beijing	2012	3.69E+14	This research
Province of Tianjin	2012	3.25E+14	This research
Urban areas of Hebei	2012	1.22E+14	This research
Province of Beijing	2012	1.08E+14	This research
Rome	2002	8.11E + 13	Ascione et al. (2009)
Taipei	1990	6.76E + 13	Huang (1998)
Province of Hebei	2012	3.83E + 13	This research

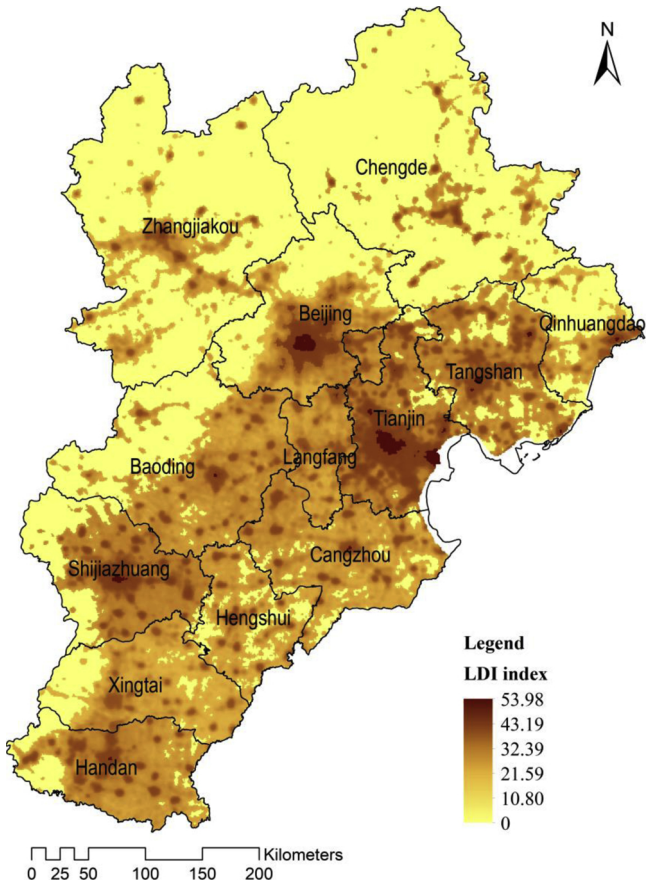

Fig. 11. Distribution of the Landscape Development Index (LDI) in the Jing-Jin-Ji region.

3.5. The human disturbance gradients map

The distribution of the LDI index of the Jing-Jin-Ji region is showed in Fig. 11. The darker spots indicate higher human disturbance to the ecosystem.

Table 5 shows the LDI indices for each city in the Jing-Jin-Ji region. The average LDI of Beijing is the fourth lowest among 13 cities, just slightly higher than Chengde, Zhangjiakou and Qinhuangdao, and significantly lower than its neighbors Tianjin and Langfang, which can be an evidence that some of the high energy consumed industries have moved out of Beijing to neighboring cities. Tianjin and Langfang have the highest average LDI (32.54 and 30.25) and the lowest spatial variation coefficient (SVC) (31% and 15%), indicating that the human disturbance of the environment is large, and the area developed and utilized by humans is large and uniform. Chengde and Zhangjiakou have the lowest LDI average (3.94 and 6.06) and the highest SVC (257% and 195%), indicating that human disturbance is relatively small but uneven, which means that some zones are characterized by high human disturbance degree in an overall relatively low human disturbance background.

Table 5
Statistical results of the Landscape Development Index (LDI) of each city in the Jing-Jin-Ji region.

City	Cell count	Minimum	Maximum	Mean	Standard deviation	SVC %
Tianjin	18192	0	56.23	34.81	10.70	31%
Langfang	9643	0	47.35	32.83	5.33	16%
Tangshan	21055	0	51.29	28.73	13.94	49%
Cangzhou	21211	0	47.24	28.27	9.84	35%
Handan	17457	0	50.33	27.83	12.81	46%
Shijiazhuang	20800	0	53.72	25.30	16.82	66%
Xingtai	18188	0	41.47	24.54	12.91	53%
Hengshui	13009	0	44.85	23.82	12.94	54%
Baoding	33263	0	47.53	20.44	16.38	80%
Beijing	24979	0	50.94	20.37	17.71	87%
Qinhuangdao	11953	0	47.30	14.02	16.16	115%
Zhangjiakou	56578	0	44.02	6.14	12.00	195%
Chengde	61166	0	47.17	4.19	10.82	259%

Table 6 shows the results of the overlay analysis of the LDI map and the land-use map. Residential and constructive area have the highest LDI average (30.13) and the lowest SVC (35%), indicating that these areas have the highest intensity in human disturbance but evenly distributed energy and resource consumption patterns. Forestland and Grassland have the lowest LDI averages (4.51 and 6.91) and the highest SVCs (234% and 183%). This shows that although the overall level of human disturbances in grassland and forestland is low, there are significant differences in the level of disturbances. Some areas have LDI values as high as 49.35 and 52.52. Cropland and water area also show high human disturbance levels (LDI averages are 21.57 and 22.29). Some of the areas where outside residential and constructive areas that show LDI values almost as high as residential and constructive areas. On the one hand, it can be explained that some non-residential and constructive areas are also severely interfered by humans. On the other hand, it may technically due to the blooming effect of DMSP-OLS light data. Blooming effect means that the lit areas extend beyond the source's true illuminated area, mainly because of the limited resolution and the producing procedure of the imagery (averaging the adjacent input cells to produce output cell) (Bennett and Smith, 2017). It is not difficult to understand that the lights of one area do not exactly light inside the boundary. It definitely will illuminate adjacent areas (include cropland, grassland, water area, etc.) through the light transmission. This issue is more pervasive over water and snow areas, as these reflect nearby lights more than dark ground (Xie et al., 2014). This problem is quite troublesome when studying cities because it can result in overestimation of features such as urban extent (Small and Elvidge, 2013). However, when we studying the human disturbance in the landscape, not only do we not think that it is a problem, but we consider that it is a good indicator that reflects the spatial extent of human disturbance. Because the human disturbance of the ecosystem is probably not exactly inside the human settlements boundary as the land use map shows. Human activities inside the residential and constructive area may affect the adjacent cropland, water area, grassland and forest. The human lights that intrude into the adjacent land can reflect the impact of human activities that penetrated to other land use types.

3.6. Limitations

There are several limitations to this study. Regarding the renewable emergy, due to the data availability, some spatial data are only long-term average values, rather than specific values for the resource flow per year (i.e. geothermal energy, wind speed, solar radiation, and evapotranspiration). In addition, some of the distribution maps are obtained by interpolation of monitoring data, and the resolution of some satellite-based data is fairly low, which may cause some uncertainties. These limitations will be minimized with the improvement of monitoring and mapping technology, and then people could retrieve better datasets. Another limitation is the transformities of renewable resources used in this study. Transformities of a specific energy flow can vary based on the processes or location (Lee and Brown, 2018). We used transformities from latest literature, however, it is well understood that transformities at the local scale may vary from the global average data.

The main limitation encountered regarding the spatialization of non-renewable emergy emerged from the saturation correction method. A linear regression model was applied to modify the 2010–2011 radiance calibration image in order to minimize the differences between its lights data and the stable lights data in 2012. It is assumed that the

Table 6
Overlay analysis of the Landscape Development Index (LDI) map and the land-use map.

LUCC ID	Land use type	Cell count	Minimum	Maximum	Mean	Standard deviation	SVC %
1	Cropland	151373	0	50.79	23.40	15.10	65%
2	Forestland	69512	0	51.61	4.80	11.37	237%
3	Grassland	51909	0	54.82	7.42	13.68	184%
4	Water area	10187	0	55.86	24.24	15.98	66%
5	Residential and constructive area	40139	0	56.23	32.76	11.38	35%
6	Unused land	2469	0	42.46	13.24	16.29	123%

actual light radiation in the saturated part in stable lights image changed as the same mode as the unsaturated part between the two data. However, there is no available data to confirm that the actual radiation of the saturated lights in the urban centers of the Jing-Jin-Ji region changes like that mode. Some researchers consider that since most of the cities in China are still in rapid development, the actual radiation changes over time in light saturated areas of urban centers might be unpredictable (Ma et al., 2014). But we are more willing to believe that it is not significant in one or two years.

4. Conclusions

Emergy is a measure of environmental support from an energy perspective that goes into the system. It provides a quantitative way of measuring the global and the local impact on the environment. The impact of cities goes far beyond its boundary because it must bring resources from all over the planet to support its development. The impact globally can be measured by the quantity of emergy necessary to support it, and the impact of locally can be measured by the LDI.

In this study, we developed a method to spatialize a high-resolution (30 arc second) emergy distribution map of a region, through which we can identify the hot spots of emergy use, spatial patterns of emergy flows, and human disturbance gradients, etc., which can monitor and map human activities and development, and guide for more accurate and specific sustainable planning strategy that break through the limits of administrative boundaries. Based on GIS technologies and environmental geospatial databases, it is feasible to generate maps of the spatial distribution of renewable emergy. Due to the availability of statistical data, non-renewable emergy distribution map for a region usually display in administrative boundary patched way. Nighttime lights data is an applicable proxy for spatializing non-renewable emergy, which can further improve the spatial detail of emergy mapping. It is noteworthy that the saturation correction for DMSP-OLS data is crucial, especially in urban areas, in order to study the spatial thermodynamics of a region better.

From the case study of Jing-Jin-Ji region, we can conclude that the empower density and LDI maps of cities for the year 2012 can be evidences of development status and policies implemented in the past. As municipalities, Beijing and Tianjin were most developed, while cities in Hebei were far away behind. Before and after 2008 Olympics, in order to ensure good environment conditions for the Beijing, large numbers of Beijing's industrial enterprises migrated outward, mainly to areas in neighboring cities such as Tianjin, Langfang, Tangshan and Cangzhou (Zhang et al., 2014a, b). At the same time, the upper reaches of Beijing, areas in Chengde and Zhangjiakou, strictly controlled industrial development and protected the environment (Zhang, 2009). Long-term research will better interpret the changes and transmissions of spatial thermodynamics of a region, which is one of the future study scopes. Meanwhile, from the LDI and land use map we found that some areas of cropland, water area, grassland and forest are suffering acute human disturbance, which indicates that the real human disturbance can extend beyond the human settlements area that mapped in land use map. The blooming effect of DMSP-OLS data may help to measure the real human disturbance spatial extent, which is also one of the interesting points for further research.

Acknowledgments

This work is supported by the Projects of Sino-Italian Cooperation of China Natural Science Foundation (CNSC, No. 7171101135) and the Italian Ministry of Foreign Affairs and International Cooperation (MAECI, High Relevance Bilateral Projects), National Key R&D Program of China (No. 2016YFC0503005), National Natural Science Foundation of China (Grant No. 71673029) and the 111 Project (No. B17005). Luca Coscieme is funded by an IRC/Marie Skłodowska-Curie CAROLINE Postdoctoral Fellowship (IRC-CLNE/2017/567).

Appendix A

Table A1–A3

Table A1
Ranking of total renewable emergy of cities in the Jing-Jin-Ji region.

Rank	City	Total Renewable emergy(sej/yr)
1	Zhangjiakou	1.80E + 21
2	Chengde	1.66E + 21
3	Baoding	4.97E + 20
4	Cangzhou	4.66E + 20
5	Beijing	4.32E + 20
6	Tangshan	4.25E + 20
7	Tianjin	3.59E + 20
8	Handan	3.36E + 20
9	Xingtai	3.26E + 20
10	Shijiazhuang	2.96E + 20
11	Qinhuangdao	2.91E + 20
12	Hengshui	2.62E + 20
13	Langfang	1.71E + 20

Table A2
Ranking of average density of renewable empower of cities in the Jing-Jin-Ji region.

Rank	City	Average density of renewable empower(sej m^{-2} yr^{-1})	Standard Deviation(sej m^{-2} yr^{-1})
1	Zhangjiakou	4.80E + 10	1.92E + 10
2	Chengde	4.10E + 10	1.53E + 10
3	Qinhuangdao	3.68E + 10	9.23E + 09
4	Cangzhou	3.32E + 10	3.59E + 09
5	Hengshui	3.05E + 10	2.65E + 09
6	Tangshan	3.05E + 10	5.67E + 09
7	Tianjin	2.98E + 10	5.01E + 09
8	Handan	2.90E + 10	2.23E + 09
9	Xingtai	2.70E + 10	3.80E + 09
10	Langfang	2.69E + 10	3.02E + 09
11	Beijing	2.61E + 10	5.84E + 09
12	Baoding	2.26E + 10	4.65E + 09
13	Shijiazhuang	2.15E + 10	3.29E + 09

Table A3
Ranking of average density of renewable empower of different land use types in the Jing-Jin-Ji region.

Rank	Land use type	Average density of renewable empower(sej m^{-2} yr^{-1})	Standard Deviation(sej m^{-2} yr^{-1})	Proportion of area
1	Unused land	5.38E + 10	2.08E + 10	0.8%
2	Forestland	3.64E + 10	1.38E + 10	21.4%
3	Grassland	3.62E + 10	1.59E + 10	15.9%
4	Cropland	3.28E + 10	1.42E + 10	46.3%
5	Water area	3.26E + 10	1.04E + 10	3.3%
6	Residential and constructive area	2.84E + 10	8.44E + 09	12.4%

Appendix B

Table B1

Table B1
Global Moran's I index confidence levels for z-scores and p-values.

z-score	p-value	Confidence level
< -1.65 or $> +1.65$	< 0.10	90%
< -1.96 or $> +1.96$	< 0.05	95%
< -2.58 or $> +2.58$	< 0.01	99%

Appendix C

Table C1

Table C1
Ranking of the Global Moran's *I* index of total emergy use in the cities of Jing-Jin-Ji region.

Rank	City	Global Moran's I index	p-value	z-score
1	Beijing	0.982850	< 0.001	189.36
2	Tianjin	0.962132	< 0.001	182.08
	Entire region	*0.960069*	*< 0.001*	*526.24*
3	Qinhuangdao	0.937601	< 0.001	91.85
4	Xingtai	0.928995	< 0.001	123.02
5	Baoding	0.927779	< 0.001	152.29
6	Shijiazhuang	0.916810	< 0.001	135.27
7	Zhangjiakou	0.912476	< 0.001	131.18
8	Chengde	0.904396	< 0.001	109.21
9	Tangshan	0.896106	< 0.001	168.93
10	Langfang	0.885826	< 0.001	119.86
11	Hengshui	0.881600	< 0.001	93.73
12	Cangzhou	0.879299	< 0.001	136.00
13	Handan	0.861942	< 0.001	125.27

References

Amaral, S., Câmara, G., Monteiro, A.M.V., Quintanilha, J.A., Elvidge, C.D., 2005. Estimating population and energy consumption in Brazilian Amazonia using DMSP night-time satellite data. Comput. Environ. Urban Syst. 29, 179–195.

Arbault, D., Rugani, B., Tiruta-Barna, L., Benetto, E., 2014. A first global and spatially explicit emergy database of rivers and streams based on high-resolution GIS-maps. Ecol. Modell. 281, 52–64.

Ascione, M., Campanella, L., Cherubini, F., Ulgiati, S., 2009. Environmental driving forces of urban growth and development An emergy-based assessment of the city of Rome, Italy. Landscape Urban Plann. 93, 238–249.

Bennett, M.M., Smith, L.C., 2017. Advances in using multitemporal night-time lights satellite imagery to detect, estimate, and monitor socioeconomic dynamics. Remote Sens. Environ. 192, 176–197.

Brown, M.T., Ulgiati, S., 2016. Emergy assessment of global renewable sources. Ecol. Modell. 339, 148–156.

Brown, M.T., Vivas, M.B., 2005. Landscape development intensity index. Environ. Monit. Assess. 101, 289–309.

Brown, M.T., Campbell, D.E., De Vilbiss, C., Ulgiati, S., 2016. The geobiosphere emergy baseline: a synthesis. Ecol. Modell. 339, 92–95.

Carey, R.O., Migliaccio, K.W., Li, Y., Schaffer, B., Kiker, G.A., Brown, M.T., 2011. Land use disturbance indicators and water quality variability in the Biscayne Bay Watershed, Florida. Ecol. Indic. 11, 1093–1104.

Chand, T.R.K., Badarinath, K.V.S., Elvidge, C.D., Tuttle, B.T., 2009. Spatial characterization of electrical power consumption patterns over India using temporal DMSP-OLS night-time satellite data. Int. J. Remote Sens. 30, 647–661.

Chen, X., 2015. Explaining subnational infant mortality and poverty rates: what can we learn from night-time lights? Spat. Demography 3, 27–53.

Coscieme, L., Pulselli, F.M., Bastianoni, S., Elvidge, C.D., Anderson, S., Sutton, P.C., 2014. A thermodynamic geography: night-time satellite imagery as a proxy measure of emergy. Ambio 43, 969–979.

Coscieme, L., Sutton, P.C., Anderson, S., Liu, Q., Elvidge, C.D., 2016. Dark times: night-time satellite imagery as a detector of regional disparity and the geography of conflict. GIsci. Remote Sens. 54, 118–139.

Davies, J.H., 2013. Global map of solid earth surface heat flow. Geochem. Geophys. Geosyst. 14, 4608–4622.

Doll, C.N.H., 2008. CIESIN Thematic Guide to Night-time Light Remote Sensing and Its Applications.

Doll, C.N.H., Muller, J.-P., Elvidge, C.D., 2000. Night-time imagery as a tool for global mapping of socioeconomic parameters and greenhouse gas emissions. Ambio 29, 157–162.

Elvidge, C.D., Baugh, K.E., Hobson, V.R., Kihn, E.A., Kroehl, H.W., 1996. Detection of Fires and Power Outages Using DMSP-OLS Data. Sleeping Bear Press, Chelsea, MI, pp. 123–135.

Elvidge, C.D., Baugh, K.E., Kihn, E.A., Kroehl, H.W., Davis, E.R., 1997a. Mapping city lights with nighttime data from the DMSP operational linescan system. Photogramm. Eng. Remote Sens. 63, 727–734.

Elvidge, C.D., Baugh, K.E., Kihn, E.A., Kroehl, H.W., Davis, E.R., Davis, C.W., 1997b. Relation between satellite observed visible-near infrared emissions, population, economic activity and electric power consumption. Int. J. Remote Sens. 18, 1373–1379.

Elvidge, C.D., Baugh, K., Dietz, J.B., Bland, T., Sutton, P.C., Kroehl, H.W., 1999. Radiance calibration of DMSP-OLS low-light imaging data of human settlements. Remote Sens. Environ. 68, 77–88.

Elvidge, C.D., Imhoff, M.L., Baugh, K.E., Hobson, V.R., Nelson, I., Safran, J., Dietz, J.B., Tuttle, B., 2001. Night-time lights of the world: 1994–1995. ISPRS J. Photogramm. Remote Sens. 56, 81–99.

Elvidge, C.D., Cinzano, P., Pettit, D.R., Arvesen, J., Sutton, P., Small, C., Nemani, R., Longcore, T., Rich, C., Safran, J., Weeks, J., Ebener, S., 2007a. The Nightsat mission concept. Int. J. Remote Sens. 28, 2645–2670.

Elvidge, C.D., Tuttle, B.T., Sutton, P.C., Baugh, K.E., Howard, A.T., Milesi, C., Bhaduri, B.L., Nemani, R., 2007b. Global distribution and density of constructed impervious surfaces. Sensors 7, 1962–1979.

Elvidge, C.D., Sutton, P.C., Ghosh, T., Tuttle, B.T., Baugh, K.E., Bhaduri, B., Bright, E., 2009. A global poverty map derived from satellite data. Comput. Geosci. 35, 1652–1660.

Elvidge, C.D., Baugh, K.E., Zhizhin, M., Hsu, F.-C., 2013. Why VIIRS data are superior to DMSP for mapping nighttime lights. Proceedings of the Asia-Pacific Advanced Network. pp. 62–69.

Falchi, F., Cinzano, P., Dan, D., Kyba, C.C.M., Elvidge, C.D., Baugh, K., Portnov, B.A., Rybnikova, N.A., Furgoni, R., 2016. The new world atlas of artificial night sky brightness. Sci. Adv. 2, e1600377.

Fang, C., Ren, Y., 2017. Analysis of emergy-based metabolic efficiency and environmental pressure on the local coupling and telecoupling between urbanization and the eco-environment in the Beijing-Tianjin-Hebei urban agglomeration. Sci. China Earth Sci. 60, 1083–1097.

Garratt, J.R., 1992. The Atmospheric Boundary Layer. Cambridge University Press.

Ghosh, T., Powell, R.L., Elvidge, C.D., Baugh, K.E., Sutton, P.C., Anderson, S., 2010. Shedding light on the global distribution of economic activity. Open Geogr. J. 3.

Hara, M., Okada, S., Yagi, H., Moriyama, T., Shigehara, K., Sugimori, Y., 2004. Progress for stable artificial lights distribution extraction accuracy and estimation of electric power consumption by means of DMSP/OLS nighttime imagery. Remote. Sens. Earth Sci. 1, 31–42.

Hsu, F.-C., Elvidge, C.D., Matsuno, Y., 2013. Exploring and estimating in-use steel stocks in civil engineering and buildings from night-time lights. Int. J. Remote Sens. 34, 490–504.

Hsu, F.-C., Baugh, K., Ghosh, T., Zhizhin, M., Elvidge, C., 2015. DMSP-OLS radiance calibrated nighttime lights time series with intercalibration. Remote Sens. 7, 1855–1876.

Huang, S.-L., 1998. Urban ecosystems, energetic hierarchies, and ecological economics of Taipei metropolis. J. Environ. Manage. 52, 39–51.

Huang, S.-L., Lai, H.-Y., Lee, C.-L., 2001. Energy hierarchy and urban landscape system. Landscape Urban Plann. 53, 145–161.

Huang, S.-L., Kao, W.-C., Lee, C.-L., 2007. Energetic mechanisms and development of an urban landscape system. Ecol. Modell. 201, 495–506.

Huang, Y., Liu, G., Chen, C., Yang, Q., Wang, X., Giannetti, B.F., Zhang, Y., Casazza, M., 2018. Emergy-based comparative analysis of urban metabolic efficiency and sustainability in the case of big and data scarce medium-sized cities: a case study for Jing-Jin-Ji Region (China). J. Cleaner Prod. 192, 621–638.

Imhoff, M.L., Lawrence, W.T., Stutzer, D.C., Elvidge, C.D., 1997. A technique for using composite DMSP/OLS "City lights" satellite data to accurately map urban areas. Remote Sens. Environ. 61, 361–370.

Lee, J.M., Braham, W.W., 2017. Building emergy analysis of Manhattan: density parameters for high-density and high-rise developments. Ecol. Modell. 363, 157–171.

Lee, D.J., Brown, M.T., 2018. Renewable empower distribution of the world. J. Environ. Account. Manag in press.

Lei, K., Wang, Z., Ton, S.S., 2008. Holistic emergy analysis of Macao. Ecol. Eng. 32, 30–43.

Letu, H., Hara, M., Yagi, H., Naoki, K., Tana, G., Nishio, F., Shuhei, O., 2010. Estimating energy consumption from night-time DMPS/OLS imagery after correcting for saturation effects. Int. J. Remote Sens. 31, 4443–4458.

Letu, H., Hara, M., Tana, G., Nishio, F., 2012. A saturated light correction method for DMSP/OLS nighttime satellite imagery. IEEE Trans. Geosci. Remote Sens. 50, 389–396.

Li, X., Xu, H., Chen, X., Li, C., 2013. Potential of NPP-VIIRS nighttime light imagery for modeling the regional economy of china. Remote Sens. (Basel) 5, 3057–3081.

Li, G., Kuang, Y., Huang, N., Chang, X., 2014. Emergy Synthesis and Regional Sustainability Assessment: Case Study of Pan-Pearl River Delta in China. Sustainability 6, 5203–5230.

Lu, D., Tian, H., Zhou, G., Ge, H., 2008. Regional mapping of human settlements in southeastern China with multisensor remotely sensed data. Remote Sens. Environ. 112, 3668–3679.

Ma, L., Wu, J., Li, W., Peng, J., Liu, H., 2014. Evaluating saturation correction methods for DMSP/OLS nighttime light data: a case study from China's cities. Remote Sens. 6, 9853–9872.

Manwell, J.F., McGowan, J.G., Rogers, A.L., 2010. Wind Energy Explained: Theory, Design and Application, 2nd ed. John Wiley & Sons, New York.

Matsumura, K.-i., Hijmans, R.J., Chemin, Y., Elvidge, C.D., Sugimoto, K., Wu, W., Lee, Y.-w., Shibasaki, R., 2009. Mapping the global supply and demand structure of rice. Sustain. Sci. 4, 301–313.

Mellino, S., Ripa, M., Ulgiati, S., 2013. Spatial accounting of environmental pressure and resource consumption using night-light satellite imagery. J. Environ. Account. Manag. 1, 361–379.

Mellino, S., Ripa, M., Zucaro, A., Ulgiati, S., 2014. An emergy–GIS approach to the evaluation of renewable resource flows: a case study of Campania Region, Italy. Ecol. Modell. 271, 103–112.

Mellino, S., Buonocore, E., Ulgiati, S., 2015. The worth of land use: a GIS-emergy evaluation of natural and human-made capital. Sci. Total Environ. 506–507, 137–148.

Mitchell, A., 2005. The ESRI Guide to GIS Analysis. ESRI Press.

Odum, H.T., 1971. Environment, Power, and Society. Wiley, New York.

Odum, H.T., 1988. Self-organization, transformity, and information. Science 242, 1132–1139.

Odum, H.T., 1996. Environmental Accounting: Emergy and Environmental Decision Making. Wiley, New York.

Pulselli, R.M., 2010. Integrating emergy evaluation and geographic information systems for monitoring resource use in the Abruzzo region (Italy). J. Environ. Manage. 91, 2349–2357.

Pulselli, R.M., Rustici, M., Marchettini, N., 2007. An integrated framework for regional studies: emergy based spatial analysis of the Province of Cagliari. Environ. Monit. Assess. 133, 1–13.

Raupach, M.R., Rayner, P.J., Paget, M., 2010. Regional variations in spatial structure of nightlights, population density and fossil-fuel CO2 emissions. Energy Policy 38, 4756–4764.

Rayner, P.J., Raupach, M.R., Paget, M., Peylin, P., Koffi, E., 2010. A new global gridded data set of CO2 emissions from fossil fuel combustion: methodology and evaluation. J. Geophys. Res. 115.

Shi, K., Huang, C., Yu, B., Yin, B., Huang, Y., Wu, J., 2014a. Evaluation of NPP-VIIRS night-time light composite data for extracting built-up urban areas. Remote Sens. Lett. 5, 358–366.

Shi, K., Yu, B., Huang, Y., Hu, Y., Yin, B., Chen, Z., Chen, L., Wu, J., 2014b. Evaluating the ability of NPP-VIIRS nighttime light data to estimate the gross domestic product and the electric power consumption of china at multiple scales: a comparison with DMSP-OLS data. Remote Sens. (Basel) 6, 1705–1724.

Small, C., Elvidge, C.D., 2013. Night on Earth: mapping decadal changes of anthropogenic night light in Asia. Int. J. Appl. Earth Obs. Geoinf. 22, 40–52.

Su, M., Fath, B.D., Yang, Z., Chen, B., Liu, G., 2013. Ecosystem health pattern analysis of urban clusters based on emergy synthesis: results and implication for management. Energy Policy 59, 600–613.

Sutton, P.C., 1997. Modeling population density with night-time satellite imagery and GIS. Comput. Environ. Urban Syst. 21, 227–244.

Sweeney, S., Cohen, M., King, D., Brown, M.T., 2007. Creation of a global emergy database for standardized national emergy synthesis. Brown, M.T. (Ed.), Emergy Synthesis 4: Proceedings of the 4th Biennial Emergy Research Conference pp. 23.21-23.18.

Townsend, A.C., Bruce, D.A., 2010. The use of night-time lights satellite imagery as a measure of Australia's regional electricity consumption and population distribution. Int. J. Remote Sens. 31, 4459–4480.

Xie, Y., Weng, Q., Weng, A., 2014. A comparative study of NPP-VIIRS and DMSP-OLS nighttime light imagery for derivation of urban demographic metrics. International Workshop on Earth Observation and Remote Sensing Applications. pp. 335–339.

Yu, X., Geng, Y., Dong, H., Fujita, T., Liu, Z., 2016. Emergy-based sustainability assessment on natural resource utilization in 30 Chinese provinces. J. Cleaner Prod. 133, 18–27.

Zhang, L., 2009. Beijing Mountain Functional Zonning and relative policies. Econ. Geogr. (in Chinese) 29, 989–994.

Zhang, Q., Schaaf, C., Seto, K.C., 2013. The vegetation adjusted NTL urban index a new approach to reduce saturation and increase variation in nighttime luminosity. Remote Sens. Environ. 129, 32–41.

Zhang, G., Wang, S., Liu, S., Jia, S., 2014a. Study on co-ordination between Beijing-Tianjin-Hebei based on industry matching and transfer. Econ. Manag. (in Chinese) 28, 14–20.

Zhang, M., Liu, J.G., Zhao, X., Chen, M.M., 2014b. Assessment of the changes of wetland health based on landscape development intensity index. Res. Soil Water Conserv. (in Chinese) 21, 157–162.

Zheng, Y.F., Yin, Z.Y., Rong-Jun, W.U., Liu, J.J., 2012. Analyses on variation and cause of surface solar radiation in Beijing,Tianjin and Hebei regions from 1960 to 2005. Plateau Meteorol. (in Chinese) 31, 436–445.

Ziskin, D., Baugh, K., Hsu, F.-C., Elvidge, C.D., 2010. Methods used for the 2006 radiance lights. Proceedings of the Asia-Pacific Advanced Network. pp. 131–142.